Modeling multicellular dynamics regulated by extracellular-matrix-mediated mechanical communication via active particles with polarized effective attraction

Yu Zheng,[1,*] Qihui Fan,[2,3,*] Christopher Z. Eddy,[4] Xiaochen Wang,[2,3] Bo Sun,[4,†] Fangfu Ye,[2,3,5,‡] and Yang Jiao [6,1,§]

[1]*Department of Physics, Arizona State University, Tempe, Arizona 85287, USA*
[2]*Beijing National Laboratory for Condensed Matte Physics and CAS Key Laboratory of Soft Matter Physics, Institute of Physics, Chinese Academy of Sciences, Beijing 100190, China*
[3]*School of Physical Sciences, University of Chinese Academy of Sciences, Beijing 100049, China*
[4]*Department of Physics, Oregon State University, Corvallis, Oregon 97331, USA*
[5]*Wenzhou Institute, University of Chinese Academy of Sciences, Wenzhou, Zhejiang 325001, China*
[6]*Materials Science and Engineering, Arizona State University, Tempe, Arizona 85287, USA*

Collective cell migration is crucial to many physiological and pathological processes such as embryo development, wound healing, and cancer invasion. Recent experimental studies have indicated that the active traction forces generated by migrating cells in a fibrous extracellular matrix (ECM) can mechanically remodel the ECM, giving rise to bundlelike mesostructures bridging individual cells. Such fiber bundles also enable long-range propagation of cellular forces, leading to correlated migration dynamics regulated by the mechanical communication among the cells. Motivated by these experimental discoveries, we develop an active-particle model with polarized effective attractions (APPA) to investigate emergent multicellular migration dynamics resulting from ECM-mediated mechanical communications. In particular, the APPA model generalizes the classic active-Brownian-particle (ABP) model by imposing a pairwise polarized attractive force between the particles, which depends on the instantaneous dynamic states of the particles and mimics the effective mutual pulling between the cells via the fiber bundle bridge. The APPA system exhibits enhanced aggregation behaviors compared to the classic ABP system, and the contrast is more apparent at lower particle densities and higher rotational diffusivities. Importantly, in contrast to the classic ABP system where the particle velocities are not correlated for all particle densities, the high-density phase of the APPA system exhibits strong dynamic correlations, which are characterized by the slowly decaying velocity correlation functions with a correlation length comparable to the linear size of the high-density phase domain (i.e., the cluster of particles). The strongly correlated multicellular dynamics predicted by the APPA model is subsequently verified in *in vitro* experiments using MCF-10A cells. Our studies indicate the importance of incorporating ECM-mediated mechanical coupling among the migrating cells for appropriately modeling emergent multicellular dynamics in complex microenvironments.

I. INTRODUCTION

Cell migration in an extracellular matrix (ECM), a complex dynamic process involving a series of intracellular and extracellular activities [1,2], is crucial to many physiological and pathological processes including tissue regeneration, immune response, and cancer progression [3–6]. It has been well established that cell migration can be significantly influenced by the microenvironment via chemotaxis [7], durotaxis [8–10], haptotaxis [11], and contact guidance [12–14]. Migrating cells can generate active pulling forces via actomyosin contraction [15–17], which are transmitted to the ECM fibers through focal adhesion complexes [18–20]. The active cellular forces can mechanically remodel the local ECM, e.g., by re-orienting the collagen fibers, forming fiber bundles, and increasing the local stiffness of the ECM [21–26]. Recent studies have indicated that a delicate balance among the magnitude of the pulling forces, the cell-ECM adhesion strength, and the ECM rigidity is required to achieve an optimal mode of single-cell migration [27].

In a multicellular system, the active pulling forces generated by individual cells can propagate in the ECM [28–32] and can be sensed by distant cells [33]. This ECM-mediated mechanical coupling among the cells could further influence the migration of the individual cells, which in turn alters the ECM structure and properties, leading to a rich spectrum of collective migratory behaviors [34–37]. For example, our *in vitro* experimental study (see details in Secs. II and III) showed that highly motile MCF-10A cells migrating on a thick layer (∼2 mm) of collagen-I gel develop strongly correlated dynamics via mechanically remodeled fiber bundles bridging the migrating cells (see Fig. 1). In addition, it was

* These authors contributed equally to this work.
† sunb@physics.oregonstate.edu
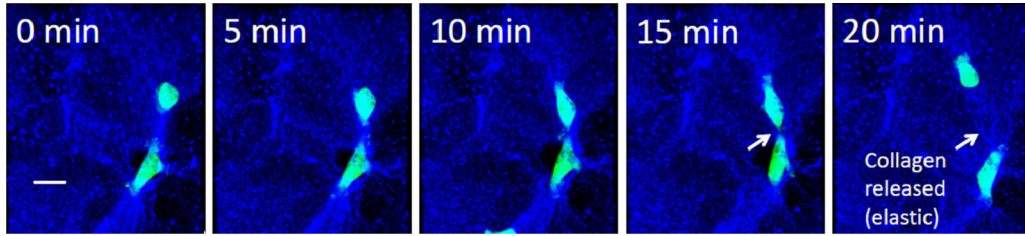‡ fye@iphy.ac.cn
§ yang.jiao.2@asu.edu

FIG. 1. Confocal microscopy images showing strongly correlated migration of a pair of MCF-10A cells (green) on thick collagen gel ($\sim$2 mm) with a collagen concentration of 2 mg/ml. The scale bar is 30 μm. The contraction of the cells at the front edge mechanically remodel the ECM, leading to the formation of fiber bundles (blue) bridging the migrating cells (green). It has been shown [36] that the fiber bundles carry significant tensile forces, thus suggesting that the observed correlated migration dynamics resulted from the mechanical communications among the cells via the remodeled fiber bundles.

shown that the fiber bundles carry significant tensile forces, thus suggesting that the observed correlated migration dynamics resulted from the mechanical communications among the cells via the remodeled fiber bundles [36].

Many computational models have been developed to investigate the individual and multicellular migration dynamics [38–40] as well as various subcellular processes involved in cell migration [41–46]. Examples include vertex-based models [47], multistate cellular Potts models [48], and cellular automaton models [49–52]. Recently, the influence of the cell-ECM interactions and/or ECM-mediated indirect cell-cell interactions on individual and collective or correlated migration dynamics started to be explicitly considered and incorporated in cell migration models [53–64]. For example, Goychuk *et al.* [55] introduced a cellular Potts model for cell migration that includes basic cell-ECM coupling. Abdel-Rahman *et al.* recently developed a computational model based on continuum mechanics that explicitly considers the micromechanical coupling of a migrating cell and the two-dimensional (2D) substrate [59] to successfully reproduce durotaxis effects. Moreover, a novel model for investigating cell migration in a model 2D ECM network guided by external mechanical cues has been developed by Dietrich *et al.* that explicitly considers the coarse-grained cytoskeleton of a migrating cell as a part of the ECM network [60]. Very recently, the 2D vertex cell model was coupled to an elastic network of springs modeling the ECM, through dynamic focal adhesion attached to the network nodes, which has been employed to understand the effect of substrate stiffness on collective migration during wound healing and to measure traction forces during cell migration [61–63]. Feng *et al.* recently developed a single-cell migration model based on mechanical coupling of a model cell and lattice model of the ECM network which has successfully reproduced the durotaxis and contact guidance effects [64].

The active-particle model is one of the most widely used models for multicellular dynamics. In the seminal work of Vicsek *et al.* [65], it was shown that local velocity correlation among neighboring active particles can induce a dynamic phase transition in the system. The Vicsek *et al.* model was subsequently generalized to include cell-cell contact interactions to investigate collective cellular dynamics such as cell sorting [66]. More recently, the active Brownian particle model (and its different variants) has received intensive

attention. In these models, a migrating cell is treated as an active particle whose dynamics is mainly determined by an active self-propelling force, a random drift, and various effective particle-particle and/or particle-environment interactions [67–69]. A wide spectrum of collective dynamics has been observed and investigated in active-particle systems [70].

In this work, motivated by the experimental observation that active pulling forces generated by migrating cells and propagated via fiber bundles can lead to strongly correlated migration dynamics [e.g., nearby cells effectively attract each other and move towards each other (see Fig. 1)], we develop an active-particle model with polarized effective attractions (APPA) for modeling emergent multicellular migration dynamics regulated by ECM-mediated mechanical communications. The APPA model generalizes the classic active-Brownian-particle (ABP) model by imposing a pairwise polarized attractive force between the migrating cells (modeled as active particles), which depends on the instantaneous dynamic states of cells including the position and velocity alignment and mimics the effective mutual pulling between the cells via the fiber bundle bridge.

The APPA model predicts enhanced aggregation behaviors compared to those predicted by the classic ABP model, and the contrast is more apparent at lower particle densities ϕ (i.e., the fraction of space covered by the particles) and higher rotational diffusivities D_r of the persistent cellular velocity. Importantly, in contrast to the classic ABP system where the particle velocities are not correlated for all ϕ, the high-density phase of the APPA system (i.e., densely packed aggregates of the particles) exhibits strong dynamic correlation, which is revealed by the velocity vector map and characterized by the slowly decaying velocity correlation functions with a correlation length (i.e., the length scale associated with the first local minimum of the function) comparable to the linear size of the high-density particle aggregate. The strongly correlated multicellular dynamics predicted by the APPA model is subsequently verified in *in vitro* experiments observing MCF-10A cells migrating on 3D collagen gels, which exhibit strongly correlated migration dynamics at high cellular densities. These results indicate the importance of incorporating ECM-mediated mechanical coupling among the migrating cells for appropriately modeling emergent multicellular dynamics in complex microenvironments.

We note that our focus here is mainly to elucidate the role of the ECM-mediated mechanical coupling in giving rise to the multicellular dynamics during the aggregation of the cells from an initial low-density dispersed state rather than investigating the collective arrangement and dynamics when the cells already form a dense cluster. In the latter case, the epithelial MCF-10A cells form stable cell-cell junctions upon mutual contact with one another, which are crucial to the collective dynamics of the dense cellular cluster and have been studied via cellular Potts models and vertex-type models. Our APPA model does not consider the effects of cell-cell adhesion upon contact and therefore is more suitable for application to investigate the initial phase of aggregation (i.e., before the formation of dense clusters), during which the cell-cell contact and the associated cell-cell junction formation are rare. In Appendix B we show that incorporating cell-cell contact adhesion does not qualitatively affect the observed dynamic correlation and aggregation behaviors.

II. METHODS

A. Active particles with polarized effective attractions

Our APPA model generalizes the classic ABP model [70] by introducing polarized attractions to model the effects of ECM-mediated mechanical coupling between the cells. In this section we describe the APPA model and its biophysical background.

Cell migration in the fibrous ECM is a complex dynamic process involving a series of intracellular and extracellular activities [1,2], which can be significantly influenced by the heterogeneity of local ECM microstructure [71–73] and mechanical properties [74–77]. A migrating cell also generates active pulling forces [15–17], which are transmitted to the ECM fibers via focal adhesion complexes [18–20]. Such active forces remodel the local ECM, e.g., by reorienting the collagen fibers, forming fiber bundles, and increasing the local stiffness of the ECM [21–26]. Importantly, the remodeled fiber bundles can efficiently transmit the active (pulling) forces generated by the cells, enabling mechanical dialogues between the migrating cells. As illustrated in Fig. 1, fiber bundles typically form between two cells migrating towards each other and connect the polarized pulling ends of the cells. This allows the pulling forces generate by one cell to propagate to and be sensed by the other cell and vice versa.

Accordingly, we phenomenologically model the effects of this mechanical dialogue here using effective attraction between the cells (see Fig. 2). Since cell velocity is typically aligned with the polarization direction, the effective attraction is also polarized (instead of being isotropic). We also note that the fiber bundles disappear as the cell polarization direction changes, e.g., when the two cells are moving away from one another (see Fig. 1). This suggests that the fiber bundles, the structural support for the effective attractions between the cells, are mainly due to elastic ECM remodeling and are temporary [37]. Therefore, in our model, we consider the polarized effective attraction only existing between a pair of migrating cells that are *moving towards each other* (see the mathematical details below). The underlying ECM network
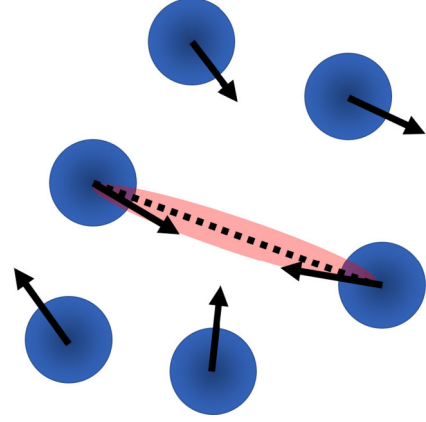

FIG. 2. Schematic illustration of the effective polarized attraction between two migrating cells, which depends on both the positions and velocities of the cells. Specifically, the effective attraction is nonzero only when the two cells are moving towards one another (i.e., with the velocities antiparallel, aligned within a prescribed tolerance).

and the remodeled fiber bundles will not be explicitly considered in our model.

Specifically, we consider the dynamics of active particles with polarized effective attractions described by the generalized overdamped Langevin equation, i.e.,

$$\dot{\mathbf{r}}_i(t) = v_0 \mathbf{e}_i + \mu \mathbf{F}_i^{\text{ECM}} + \sqrt{2D_t}\boldsymbol{\eta}_i(t), \qquad (1)$$

where the subscript i is the particle index, v_0 is the persistent speed of the particle, $\mathbf{e}_i$ is a unitary vector characterizing the persistent speed direction and subject to rotational diffusion with the diffusion coefficient D_r, D_t is the translational diffusivity of the particle, and $\boldsymbol{\eta}_i(t)$ is a unitary white noise with the correlation function $\langle \boldsymbol{\eta}_i(t) \cdot \boldsymbol{\eta}_j(t^*) \rangle = \delta_{ij}(t - t^*)$. The parameter μ is the cellular mobility and $\mathbf{F}_i^{\text{ECM}}$ is the total force due to ECM-mediated mechanical coupling among migrating cells. These model parameters are determined by cell phenotype, ECM microenvironment, and stochastic subcellular processes such as actin polymerization and cell-ECM adhesion turnover. In our subsequent simulations, we select numerical values for the model parameters (provided in Sec. III) based on experimental data of MCF-10A cells migrating on 3D collagen gels (see [78]).

We also consider that each particle (cell) possesses a hard-core exclusion volume modeled as a hard sphere with radius $R_c = 10 \ \mu$m (corresponding to the characteristics radius of the cells), which prevents the overlapping of the particles upon contact. We also note that in the case of the absence of $\mathbf{F}_i^{ECM}$, the APPA model [cf. Eq. (1)] reduces to the classic active Brownian particle model, which describes single-cell migration in a statistically homogeneous ECM (e.g., one with uniform collagen density and random fiber orientations). We note that although the primary APPA model introduced here does not explicitly consider cell-cell contact adhesion, we investigate the effects of the contact adhesion by adding an adhesive layer enclosing the cells. The details of this generalized APPA model with contact adhesion and the results are discussed in detail in Appendix B and indicate that

cell-cell contact adhesion (at least as modeled here) does not qualitatively affect the aggregation behaviors and dynamic correlations among the cells.

The total force $\mathbf{F}_i^{\text{ECM}}$ due to ECM-mediated mechanical coupling is given by

$$\mathbf{F}_i^{\text{ECM}} = \sum_j f_{ij}^a(r_{ij}, \dot{\mathbf{r}}_i, \dot{\mathbf{r}}_j)\mathbf{u}_{ij}^0, \tag{2}$$

where the sum is over all neighboring particles of particle i, $\mathbf{u}_{ij}^0$ is the unit vector pointing from particle i to j, and f_{ij}^a is the pairwise polarized attraction between particles i and j, which depends on the particle separation distance r_{ij} as well as the dynamic state of the particles (i.e., $\dot{\mathbf{r}}_i$ and $\dot{\mathbf{r}}_j$), i.e.,

$$f_{ij}^a(r_{ij}, \dot{\mathbf{r}}_i, \dot{\mathbf{r}}_j) = \begin{cases} \frac{\epsilon}{r^\alpha} & \text{for } r_{ij} > (R_i + R_j) \\ & \text{for } \frac{\dot{\mathbf{r}}_i \cdot (\mathbf{r}_j - \mathbf{r}_i)}{|\dot{\mathbf{r}}_i||(\mathbf{r}_j - \mathbf{r}_i)|} > 1 - \delta \\ & \text{for } \frac{\dot{\mathbf{r}}_j \cdot (\mathbf{r}_i - \mathbf{r}_j)}{|\dot{\mathbf{r}}_j||(\mathbf{r}_i - \mathbf{r}_j)|} > 1 - \delta \\ 0 & \text{otherwise.} \end{cases} \tag{3}$$

Here the force parameter ϵ characterizes the strength of the effective polarized attraction, which mainly depends on the cell phenotype and ECM mechanical properties; R_i and R_j are the radii of particles i and j, respectively, and δ is a threshold that quantifies the degree of antiparallel alignment of the cell velocities, which is a necessary condition for ECM-mediated mechanical coupling. This parameter can be estimated by experimentally tracking cell pairs that exhibit strongly correlated migration dynamics (see [78]). In Sec. III C we systematically investigate the effect of δ on the overall aggregation behaviors of the APPA system.

We note that the exponent α in the power-law scaling $1/r^\alpha$ characterizes the propagation and decay of the active force generated by a contractile cell in the ECM and $\alpha = 1$ for an elastic continuum. On the length scale considered here, contractile cells can be considered as force dipoles characterized by $\alpha > 1$. On the other hand, the unique force chains in the ECM promote the long-range transmission of the forces, leading to $\alpha < 1$ [32]. Thus, the extract outcome of these two opposite effects is not obvious and is difficult to quantitatively verify experimentally. Here we will use $\alpha = 1$ for subsequent simulations and explore the effects of α. As shown in [78], our simulations indicate that varying α does not qualitatively change the behavior of the system (including aggregation and dynamic correlation), although it does affect the density at which significant clustering occurs (see [78]).

Equations (1)–(3) are employed in subsequent simulations of the active particles with polarized attractions. In particular, the particles are initially randomly placed in a periodic square simulation domain without overlapping. The initial velocities of particles are randomly oriented with the same magnitude v_0. The particles are then evolved according to Eq. (1), where the velocities and positions of the particles are updated at discretized time steps dt. Specifically, the Euler-forward scheme is employed to perform numerical integration (see Appendix A for details). The updated velocity vector is rescaled to v_0 while keeping its direction, accounting for the damping effects of the ECM that is not explicitly modeled here. The persistent direction of each particle is also updated by changing it by a small angle randomly selected from the interval $[-D_r, D_r]\pi$,

due to rotational diffusion. Particle overlaps are removed by pushing each particle back by half of the overlapping distance along their center-center direction. The procedure is repeated until the stationary state of the system is achieved and the simulation is terminated.

B. Mean cluster size and velocity correlation function

We quantify the morphological evolution of the APPA systems using cluster statistics. Specifically, at a given time step, the particles are grouped into different clusters. We consider that two particles belong to the same cluster if the distance between their centers is less than a threshold, i.e., $d_{ij} < R_i + R_j + \delta d$, where δd is a numerical threshold to take into account fluctuations of cell size and shape. In our simulations, we use $\delta d = 0.1R_c$ (where R_c is the radius of the cell), based on confocal images of migrating cells.

We compute the mean cluster size [79–81] to quantify the degree of clustering or aggregation of the particles, i.e.,

$$S = \frac{\sum_{k=1}^{\infty} k^2 n_k}{\sum_{k=1}^{\infty} k n_k}, \tag{4}$$

where k is number of particles that a cluster contains. A cluster containing k particles is called a k cluster. In addition, n_k is the probability that a randomly selected cluster in the system is a k cluster, which is computed by dividing the number of k clusters by the total number of clusters. It can be seen from Eq. (4) that $S \in [0, 1]$. A large S value (e.g., $S \sim 1$) indicates that the majority of particles are contained in one or a small number of dominant clusters, while a small S value indicates that the particles in the system are scattered and the level of aggregation is low.

We also compute the rate of clustering Γ to quantify how fast the aggregation occurs in different systems. Specifically, Γ is defined as the average slope of $S(t)$ up to the time step t_s at which the stationary state is achieved, i.e.,

$$\Gamma = \frac{1}{t_s} \int_0^{t_s} S'(\tau) d\tau, \tag{5}$$

where $S'(\tau) = \frac{dS}{dt}|_{t=\tau}$ is the local slope at $t = \tau$ on the $S(t)$ curve.

In addition, we employ the velocity correlation function to quantify the correlated particle dynamics on the two-body (pair) level, i.e.,

$$C(r) = \left\langle \frac{\mathbf{u}_i \cdot \mathbf{u}_j}{|\mathbf{u}_i||\mathbf{u}_j|} \right\rangle, \tag{6}$$

where $\mathbf{u}$ is the instantaneous particle velocities, $|\cdot|$ indicates the magnitude of the vector, r is the cell-center distance between a pair of cells i and j, and $\langle \cdot \rangle$ indicates the average over all cell pairs. Perfectly correlated pair dynamics is associated with $C(r) = 1$. This is the case when the velocities of all particles are perfectly aligned, e.g., indicating that the cells are following one another during collective migration. In contrast, $C(r) = -1$ is associated with antiparallel velocities, i.e., when the cells are moving towards one another. In addition, $C(r) = 0$ indicates no correlations among the particles (migrating cells).

C. Cell migration experiment

We perform *in vitro* experiments to observe and quantify migration dynamics of MCF-10A mammary epithelial cells on top of a 3D collagen gel (∼2 mm thick) and in a 2D Petri dish (solid polystyrene substrate) as the control group. In particular, MCF-10A cells marked with green fluorescent protein (GFP) were obtained from China Infrastructure of Cell Line Resource. The culture medium of MCF-10A-GFP is Dulbecco's modified Eagle's medium-F12 (Corning) supplemented with 5% horse serum (Gibco), 1% penicillin or streptomycin (Corning), 20 ng/ml of human EGF (Gibco), 10 μg/ml of insulin (Roche Diagnostics GmbH), 100 ng/ml of cholera toxin (Sigma-Aldrich), and 0.5 μg/ml of hydrocortisone (Sigma-Aldrich).

Type I collagen extracted from rat tail tendon (Corning) was diluted and the pH was neutralized to ∼7.2. Then the collagen solution was spread on the substrate in the Petri dish and incubated at 37 °C for 30 min until polymerized into a 3D matrix with a thickness of around 2000 μm. The final collagen concentration was 2 mg/ml for the tests. The cell suspension covered the matrix and stayed in the cell incubator overnight before imaging. For a collective cell migration test, 0.5 μl of cell suspension with different concentrations of cells was dropped on top of the collagen gel or solid in the Petri dish and then incubated for 2 h before imaging.

Time-lapse images were obtained using both a confocal laser scanning microscope (CLSM) with a 25× water immersion objective and an automatic inverted fluorescent microscope (Nikon Ti-E) with a 10× objective. Both microscopes were equipped with an on-stage cell-culture incubator to provide a constant temperature of 37 °C with humidity of 5% CO_2. Collagen fibers could be imaged via the reflection mode of the CLSM as previously studied. An inverted microscope was used to observe the cell migration correlation in large populations in a 2-min time interval. Imaris software was used to reconstruct the 3D images captured from the CLSM and the tracking analysis. Repeated seeding was carried out and robust clustering behaviors were repeatedly observed. Quantitative cell tracking was carried out for representative systems, based on which the cluster statistics and velocity correlation data were collected.

We note that the MDA-MB-231 cells are typically used for collective migration experiments due to their weak cell-cell adhesion. The MDA-MB-231 cells are not used here because these cells can degrade the ECM and invade into the gel. This not only makes the observation and tracking of cell migration difficult, but also induces other mechanisms that would bias their migration. For example, the cell migration can be affected by the pore distribution in the gel, and the cells tend to follow one another along a microchannel formed by a leading cell. All these additional mechanisms would mask the influence of ECM-mediated mechanical coupling. On the other hand, MCF-10A cells can generate significant pulling during migration to remodel the ECM and remain on the surface of the collagen gel, which makes them better candidates for the present study. Our focus is the dynamics of the aggregation process from an initial disperse state during which long-time stable cell-cell contact is rare.

III. RESULTS

A. Enhanced aggregation and dynamic correlation due to long-range mechanical coupling

We employ the APPA model to investigate the correlated dynamics of multicellular systems resulting from ECM-mediated mechanical coupling, such as the MCF-10A cells migrating on 3D collagen gel. In this system, the strong motility of the MCF-10A cells can result in large active pulling forces, which propagate and influence the migration of other cells via the remodeled fiber bundles (see Fig. 1).

To demonstrate the distinct dynamics resulting from the APPA model, in particular, the polarized effective attractions that mimic the mechanical dialogues between the cells, we also simulate the system using the classic ABP model. As shown in Sec. III B, the ABP system corresponds to MCF-10A cells migrating in a 2D Petri dish, without ECM-mediated long-range mechanical coupling. Unless otherwise specified, the following parameters are used in our simulations: $v_0 = 0.5$ μm/min, $\epsilon = 10$ nN/μm, $\mu = 0.12$ μm²/nN min, and $\delta = 0.104$ (corresponding to a misalignment angle tolerance of ∼$\pi/30$). In addition, we set the translational diffusivity $D_t = 0.01$ μm²/min, which is low compared to the persistent speed and is consistent with the experimental observation that MCF-10A cells on 3D collagen exhibit strong ballisticlike motions (see [78]). We will explore two distinct values of rotational diffusivity: $D_r = 0.05$, which is estimated based on single-cell migration trajectories (see [78]), and $D_r = 0.01$, which is selected to demonstrate the enhanced aggregation behavior of the APPA model compared to the ABP model, due the ECM-mediated mechanical coupling. In Sec. III C we systematically explore the effects of D_r by constructing phase diagrams of APPA systems. The values of the model parameters are calibrated and determined based on experimental data associated with the observation of a small number of MCF-10A cells migrating on 3D collagen gel (see [78]). For each set of model parameters, five independent simulations with distinct initial configurations are carried out and the results reported are ensemble averaged over these simulations.

We first investigate the systems with high rotational diffusivity (i.e., $D_r = 0.05$). High D_r values correspond to rapid relaxing of the persistent velocities, which is known to diminish particle clustering in classic ABP systems. This can be clearly seen in the top row of Fig. 3, which shows snapshots of the classic ABP system at different particle densities $\phi \in [0.1, 0.5]$ (i.e., the fraction of the simulation box area covered by the particles). No significant particle clustering occurs until at a very high particle density $\phi = 0.5$. On the other hand, the APPA system starts to show significant aggregation behavior at intermediate densities, e.g., $\phi = 0.3$ (see the bottom row of Fig. 3). The clustering behaviors of the two different systems at varying particle densities are also quantified using time-dependent cluster statistics. The top row of Fig. 4 shows the evolution of mean cluster size S [see Eq. (4) for definition] in both the classic ABP system and the APPA system. It can be seen that S increases rapidly in the APPA system with $\phi \geqslant 0.3$ and asymptotically approaches unity, indicating the emergence of a dominant cluster containing the majority of particles in the system. This is also consistent with the results
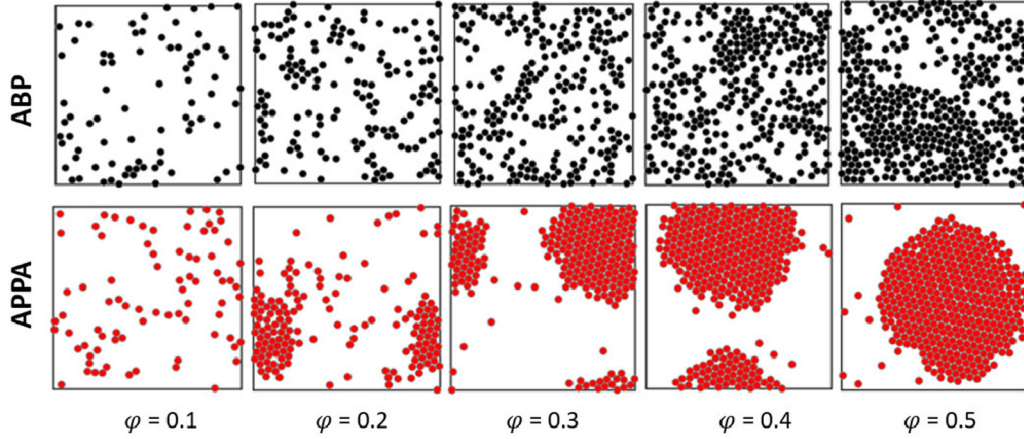
FIG. 3. Distinct aggregation behaviors at varying particle densities and high rotational diffusivity $D_r = 0.05$ rising in the classic ABP systems (top row) and in the APPA systems (bottom row). The radius of the particles is $R_c = 10 \ \mu$m and the linear size of the periodic square simulation domain is $L = 500 \ \mu$m. The particle densities from left to right are $\phi = 0.1, 0.2, 0.3, 0.4,$ and 0.5, respectively.

of the clustering rate Γ shown in the middle row. It can be seen that at lower densities ($\phi \leqslant 0.2$), the ABP and APPA systems possess similar Γ, while for $\phi \geqslant 0.3$ the APPA system exhibits much higher Γ, indicating significantly faster aggregation. We note that the APPA system at $\phi = 0.2$ exhibits interesting S dynamics, which seems to show a very low yet positive clustering rate. Although no significant aggregation behavior was observed for the duration of our simulations, which is relevant to the timescale associated with the cell

migration experiments, we cannot rule out the possibility that aggregation would eventually occur over a very long time in this system.

Importantly, the APPA system exhibits distinct dynamic correlations compared to the ABP system at high particle densities. This can be clearly seen from the velocity correlation function $C(r)$ shown in the bottom row of Fig. 4. It can be seen that $C(r) \approx 0$ for all r and all ϕ in the classic ABP system, regardless of the emergence of particle aggregation,
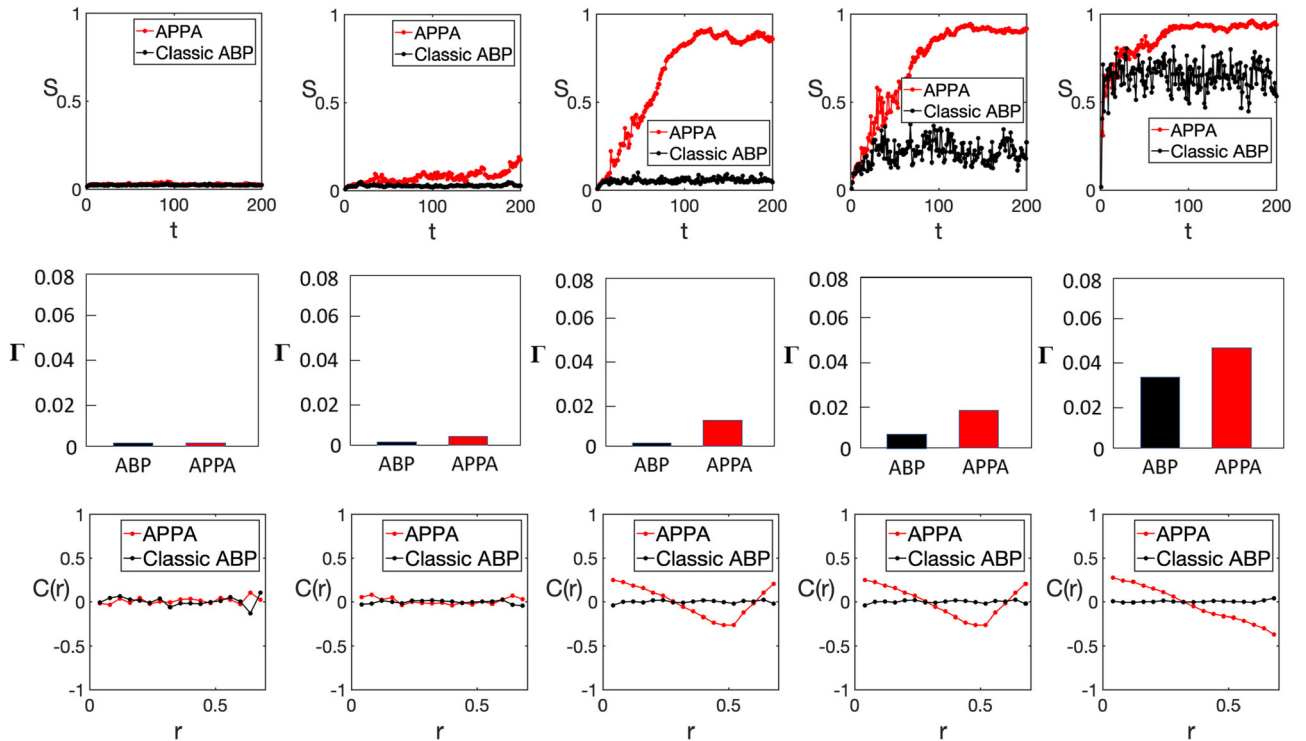

FIG. 4. Comparison of the cluster statistics S (top row) [cf. Eq. (4)], the rate of clustering Γ (middle row), and velocity correlation functions $C(r)$ (bottom row) [cf. Eq. (6)] associated with the classic ABP systems and the APPA systems at high rotational diffusivity $D_r = 0.05$ and varying particle densities. The particle densities from left to right are $\phi = 0.1, 0.2, 0.3, 0.4,$ and 0.5, respectively. The unit of time t is hours. The unit of distance r is given by the length of the square simulation box.
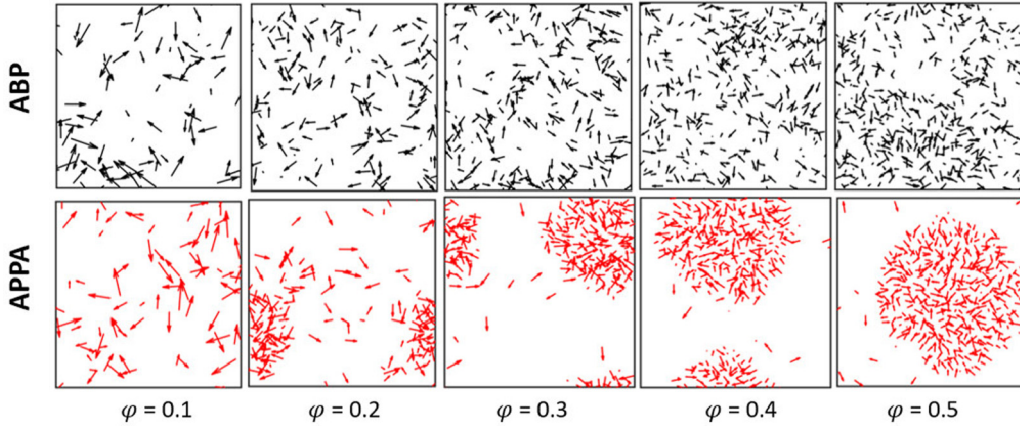
FIG. 5. Velocity maps (in which the velocity vector associated with each particle is shown as an arrow at the particle center) showing distinct velocity correlations at varying particle densities and high rotational diffusivity $D_r = 0.05$ rising in the classic ABP systems (top row) and in the APPA systems (bottom row). The particle densities from left to right are $\phi = 0.1, 0.2, 0.3, 0.4$, and 0.5, respectively.

indicating that the particles are not dynamically correlated in the system. In contrast, the APPA system exhibits strong dynamic correlations, evidenced by the slow decaying of $C(r)$, which emerges for $\phi \geqslant 0.3$, coinciding with the emergence of the particle aggregation in the corresponding system. To further understand the emergence of this dynamic correlation, we investigate the particle velocity distribution in the APPA system. Figure 5 shows the velocity maps, in which the velocity vector associated with each particle is shown as an arrow at the particle center. It can been seen that the velocities of the particles within the dominant cluster exhibit strong local and intermediate-range alignment correlation. We note that the strong velocity correlations are established during the early stage of the aggregation process, before the formation of dense clusters (see [78]). Therefore, this distinct dynamics might result from the effective polarized attractions in the APPA system.

We now investigate the systems with low rotational diffusivity $D_r = 0.01$. It is known that low D_r enhances the clustering in the classic ABP system. Indeed, as shown in the top row of Fig. 6, the ABP system starts to show enhanced

clustering behavior at $\phi = 0.4$ (as quantified by the higher clustering rate Γ compared to the $D_r = 0.05$ case) and significant aggregation is observed at $\phi = 0.5$. The enhanced clustering behavior is much more significant in the APPA system, in which a single dominant cluster emerges even at the lowest density $\phi = 0.1$. This is also quantified via the time-dependent mean cluster size S and the associated clustering rate Γ shown, respectively, in the top and middle rows of Fig. 7. Moreover, strong dynamic correlations are observed in the APPA system for all particle densities $\phi \in [0.1, 0.5]$, which is consistent with the emergence of particle clusters at low densities. The dynamic correlations can be clearly seen in the velocity maps (see Fig. 8) and the corresponding slow decay in the velocity correlation functions $C(r)$ shown in the bottom row of Fig. 7.

These results indicate that the polarized effective attraction mimicking the influence of the mechanical dialogue among the cells can lead to significantly enhanced dynamic correlations among particles. We note that enhanced clustering behavior is also nontrivial since the effective attraction is not isotropic but depends on the direction of the velocities of the
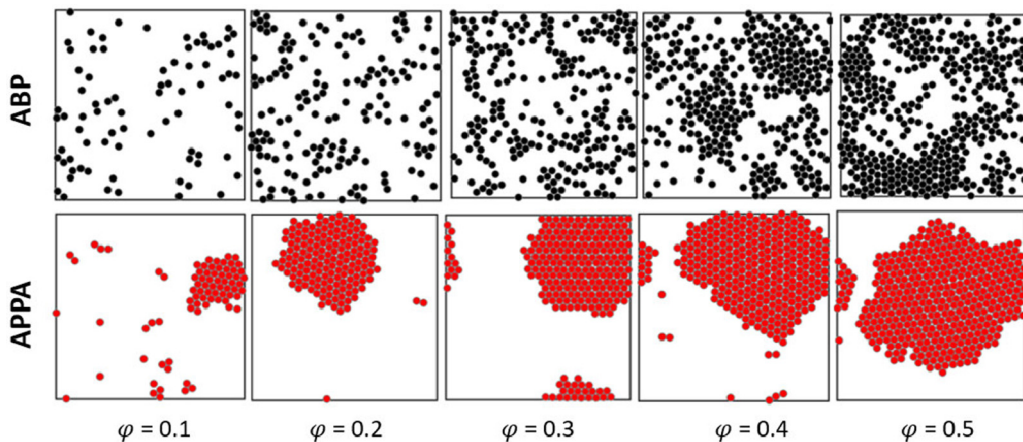

FIG. 6. Distinct aggregation behaviors at varying particle densities and low rotational diffusivity $D_r = 0.01$ rising in the classic ABP systems (top row) and in the APPA systems (bottom row). The radius of the particles is $R_c = 10 \ \mu$m and the linear size of the periodic square simulation domain is $L = 500 \ \mu$m. The particle densities from left to right are $\phi = 0.1, 0.2, 0.3, 0.4$, and 0.5, respectively.
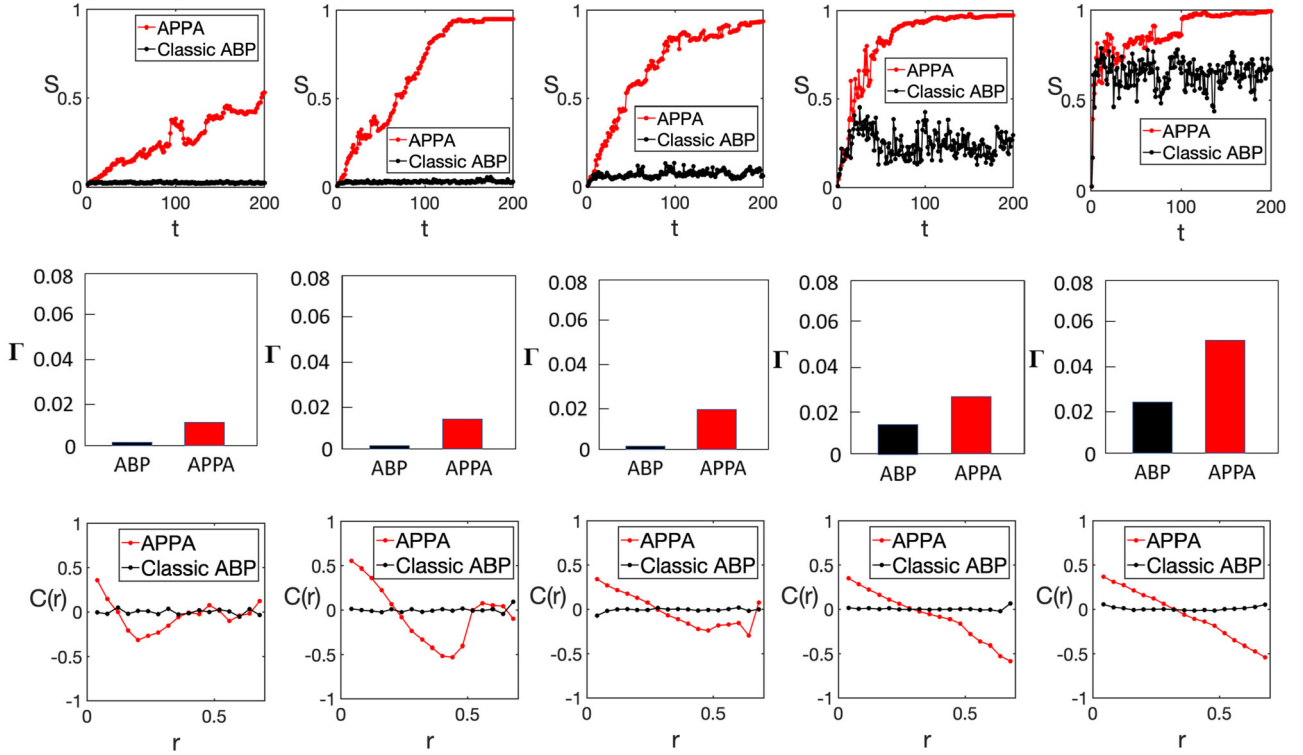
FIG. 7. Comparison of the cluster statistics S (top row) [cf. Eq. (4)], the rate of clustering Γ (middle row), and velocity correlation functions $C(r)$ (bottom row) [cf. Eq. (6)] associated with the classic ABP systems and the APPA systems at low rotational diffusivity $D_r = 0.01$ and varying particle densities. The particle densities from left to right are $\phi = 0.1, 0.2, 0.3, 0.4$, and 0.5, respectively. The unit of time t is hours. The unit of distance r is given by the length of the square simulation box.

cells. In the next section we verify these model predictions using *in vitro* experiments.

B. Experimental verification via MCF-10A cells on 3D collagen gel

To test the predictions of the APPA model, we observe *in vitro* the migration of multiple MCF-10A cells on 3D collagen I hydrogel with a collagen concentration of 2 mg/ml and thickness of ~2 mm. Single-cell migration dynamics is ac-

quired by recording and analyzing cell trajectories after a 12-h culture (see Sec. II for details). The fibrous microstructure of collagen gels can support long-range force propagation, which is crucial to mechanical signaling among the cells. The strong motility of the MCF-10A cells can generate significant contractile forces during migration and thus potentially induce strong cell-ECM mechanical coupling.

We randomly distribute the MCF-10A cells on a collagen-based ECM with two distinct cell densities, i.e., ~10^4 and 5×10^4 cells/cm^2, corresponding to the simulation values,
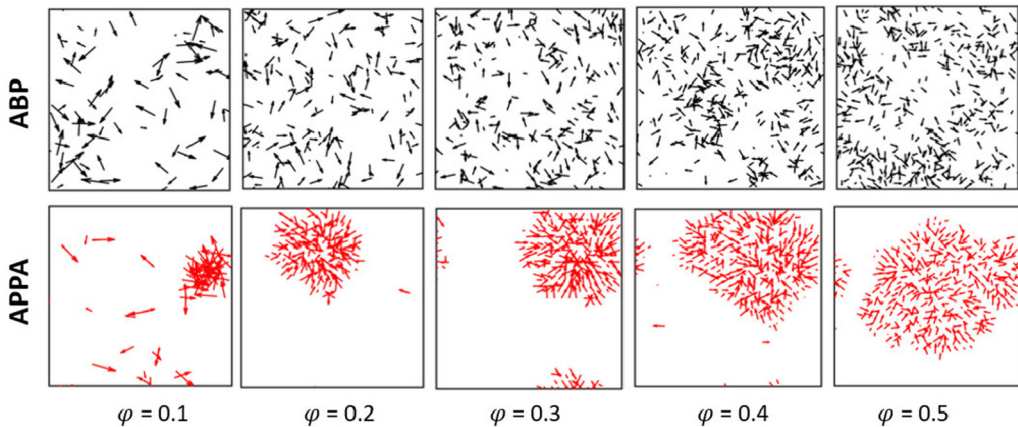

FIG. 8. Velocity maps (in which the velocity vector associated with each particle is shown as an arrow at the particle center) showing distinct velocity correlations at varying particle densities and low rotational diffusivity $D_r = 0.01$ rising in the classic ABP systems (top row) and the APPA systems (bottom row). The particle densities from left to right are $\phi = 0.1, 0.2, 0.3, 0.4$, and 0.5, respectively.
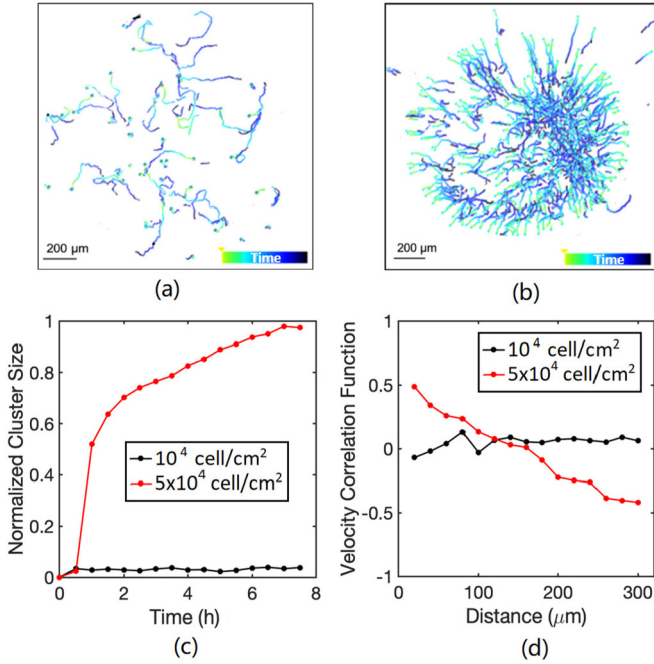
FIG. 9. Verification of the predicted enhanced aggregation and dynamic correlation in the APPA system using *in vitro* experiments of MCF-10A cells on 3D collagen gels. Tracked cell trajectories, associated with two densities (a) $\sim 10^4$ cells/cm^2 and (b) 5×10^4 cells/cm^2, correspond to the simulation values (i.e., $\phi \approx 0.1$ and 0.5, respectively) for 6 h after initial seeding. The color of the trajectory (from yellow to dark blue) reflects the tracking time. It can be seen that the trajectories in the low-density system are largely uncorrelated, while the cell migration in the high-density systems exhibits strong correlation and an overall centripetal motion consistent with the APPA model predictions. (c) Evolution of the mean cluster size S, which clearly indicates aggregation behavior at high cellular density. (d) Velocity correlation function $C(r)$, where the slower decay at high cellular density indicates the stronger correlated dynamics resulting from the collective centripetal migration mode.

i.e., $\phi \approx 0.1$ and 0.5, respectively. We observe rapid and strong aggregation in the high-density system while the cells in the low-density system remain separated [see Fig. 9(a) and 9(b)]. In particular, Figs. 9(a) and 9(b) show, respectively, the tracked cells trajectories associated with these two distinct cell densities for 6 h. It can be seen clearly that in both cases, the MCF-10A cells exhibit strong motility. In the low-density case [Fig. 9(a)], the cell migration is largely uncorrelated. In contrast, the cell migration in the high-density case [Fig. 9(b)] is strongly correlated, exhibiting an overall centripetal motion leading to aggregation. This collective dynamics is in good qualitative agreement with the APPA model predictions.

We also compute the cluster statistics S [Fig. 9(c)] as well as the velocity correlation functions $C(r)$ [Fig. 9(d)], based on the trajectory data via cell tracking. Consistent with the simulation results, the cells within the cluster in the high-density system exhibit strong dynamic correlations, as indicated by the long-range slowly decaying $C(r)$, as well as the strong centripetal migration dynamics. The cells in the low-density system are largely uncorrelated, evidenced by the flat velocity correlation function and the random cell motions.

To further verify the role of ECM-mediated mechanical coupling, we carry out control experiments by observing MCF-10A cells in a 2D Petri dish. Specifically, the cells are initially randomly distributed on solid polystyrene substrate with a number density $\sim 5 \times 10^4$ cells/cm^2, and the substrate is not able to transmit active cellular forces over long distances. As shown in Fig. 10(a), no significant collective dynamics or clustering behaviors are observed during the 6-h tracking. In fact, the cells only exhibit random motions near their original positions. The evolutions of the mean cluster size S and the velocity correlation function $C(r)$ are shown in Figs. 10(b) and 10(c), respectively, both of which indicate no significant aggregation or correlations among the migrating cells. These results clearly indicate the significant role of the ECM-mediated mechanical coupling in the observed enhanced aggregation and dynamic correlations of MCF-10A cells on 3D collagen gel.

C. Phase diagram of active particles with polarized attractions

The results in previous sections indicate that the polarized effective attractions may play an important role in giving rise to unique collective dynamics in multicellular systems (such as the strong dynamic correlation within cell aggregates). In an actual multicell-ECM system, the cell phenotype, ECM microstructure, and physical properties can all affect the active force transmission and thus the effective attraction in our model. In this section we systematically vary the key model parameter δ [cf. Eq. (3)] that determines the region of influence of the polarized forces and investigate its effects on the overall aggregation behavior and collective dynamics of the system.

In particular, for each δ, we map the observed collective behaviors of the APPA system at different rotational diffusivity $D_r \in [0.01, 0.16]$ and particle density $\phi \in [0.1, 0.5]$ to a phase diagram, where the aggregation or clustering phase and dispersion or scattered phase are distinguished. Note that the particles in the aggregation phase also possess strong dynamic correlations. Figure 11 shows the phase diagrams of the APPA system for varying δ, D_r, and ϕ. For a given δ, the aggregation phase emerges at relatively low D_r and high ϕ. We note that the classic ABP model can be obtained by setting $\delta = 0$. By increasing δ, i.e., the force influence region, the aggregation-dispersion phase boundary is pushed to higher D_r and lower ϕ, indicating enhanced aggregation behaviors due to mechanical communication. We note that the largest δ considered here corresponds to a misalignment angle tolerance of $\pi/20$, which is still relatively small. The numerical data including the cluster statistics for generating the phase diagrams are provided in [78]. We note that one possible way to experimentally vary the influence range of the ECM-mediated mechanical coupling is to systematically control and engineer the EMC microstructure, including the mesh density, fiber lengths, pore size [82,83], and fiber orientations [84].

IV. CONCLUSION

Motivated by recent experimental evidence that ECM-mediate mechanical coupling among migration cells regulates their collective dynamics, we have developed an
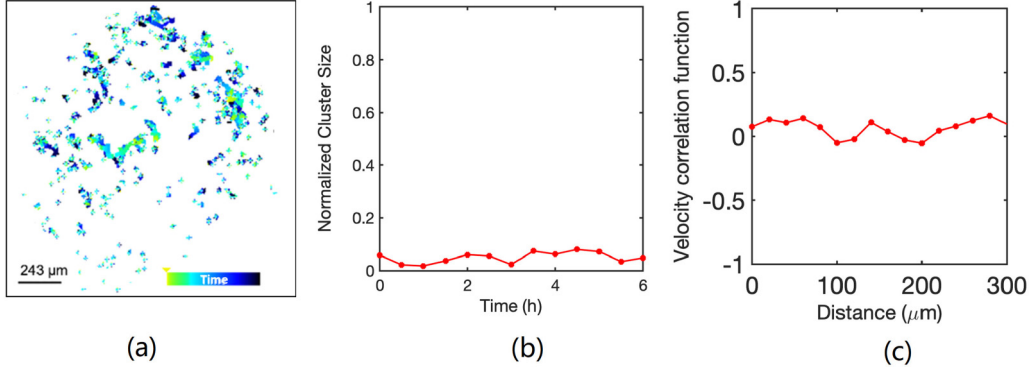
FIG. 10. (a) MCF-10A cells in a 2D Petri dish (solid polystyrene substrate) with a number density $\sim 5 \times 10^4$ cells/cm^2. The substrate is not able to transmit active cellular forces over long distances. No significant collective dynamics or clustering behaviors are observed in the 6-h tracking. The cells only exhibit random motions near their original positions. Also shown are (b) the evolution of the mean cluster size S and (c) the velocity correlation function $C(r)$, both of which indicate no significant aggregation or correlations among the migrating cells.

active-particle model with polarized effective attractions, which generalizes the classic active-Brownian-particle model. Specifically, in the APPA model, pairwise polarized attractive forces are imposed between the particles moving towards one another, which mimics the effective mutual pulling between the cells via the fiber bundle bridge. The APPA system exhibits enhanced aggregation behaviors compared to the classic ABP system, and the contrast is more apparent at lower particle densities ϕ and higher rotational diffusivities D_r. Importantly, in contrast to the classic ABP system where the particle velocities are not correlated for all particle densities, the high-density phase of the APPA system exhibits strong dynamic correlation, which is characterized by the slowly decaying velocity correlation functions $C(r)$ with a correlation length comparable to the linear size of the high-density phase domain (i.e., the cluster of particles).

We validated our model by qualitatively reproducing the collective dynamics of MCF-10A breast cancer cells migrating on 3D collagen gels, including the enhanced aggregation behaviors and strongly correlated multicellular migration dynamics, which result from the ECM-mediated mechanical coupling among the migrating cells. Our study indicates the importance of incorporating ECM-mediated mechanical coupling among the migrating cells for appropriately modeling emergent multicellular dynamics in complex microenvironments.

Although currently focusing on 2D multicellular systems (e.g., nonmetastatic MCF-10A breast cancer cells migrating on top of a 3D ECM), our model can be readily generalized to investigate the migration of mesenchymal cells (e.g., invasive MDA-MB-231 breast cancer cells) in a 3D ECM. The key modification is to explicitly incorporate the effects of ECM degradation by the cells, which leads to microchannels that bias cell migration in addition to the ECM-mediated mechanical coupling. In addition, the effects of chemotaxis and cell-cell adhesion can also be incorporated into the model to investigate a wide range of cell lines with different phenotypes.

Finally, we note that the APPA model is a simple phenomenological model that generalizes the ABP model by incorporating pairwise polarized attractions mimicking the effects of ECM-mediated mechanical couplings. In principle, this ECM-mediated mechanical coupling can be directly modeled by explicitly considering the fiber network microstructure
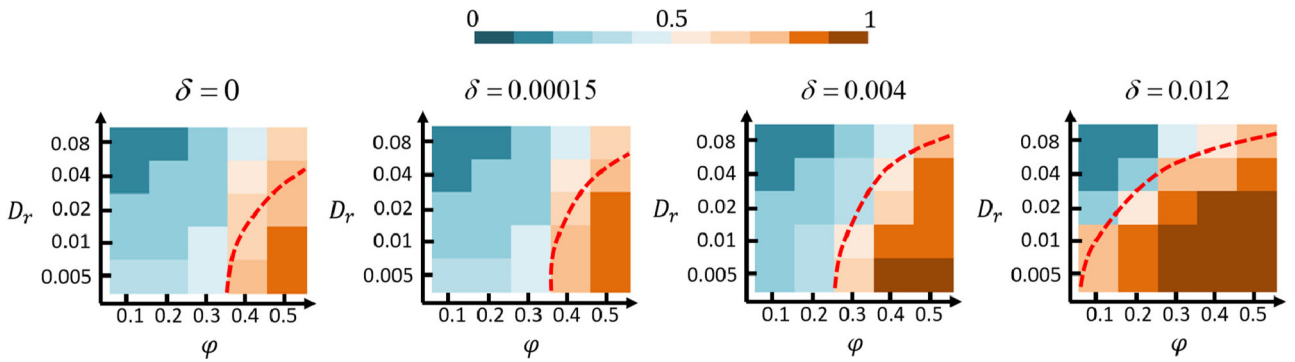

FIG. 11. Phase diagrams of the APPA system for varying δ, D_r, and ϕ. Each diagram is associated with a fixed δ, and collective behaviors of the APPA system at different rotational diffusivity $D_r \in [0.01, 0.16]$ and particle density $\phi \in [0.1, 0.5]$ are mapped to two distinct phase regions, i.e., the aggregation or clustering phase and dispersion or scattered phase. The colors indicate the values of mean cluster size S. Increasing δ (i.e., the region of influence of the polarized attractions) leads to enhanced aggregation or clustering behavior and thus stronger dynamic correlation in the aggregation phase. From left to right, $\delta = 0$, 0.00015, 0.004, and 0.012, respectively corresponding to misalignment angle tolerance of 0, $\pi/180$, $\pi/36$, and $\pi/20$. We note that the classic ABP model is associated with $\delta = 0$.

of the ECM as well as the mechanical coupling of migration cells and ECM fibers via focal adhesion complexes [36]. However, the computational cost for the latter would be significantly higher than the APPA model and it is challenging to employ it for modeling large multicellular systems.

APPENDIX A: NUMERICAL INTEGRATION SCHEME FOR SOLVING THE OVERDAMPED LANGEVIN EQUATION

Here we present the numerical schemes for integrating the stochastic Langevin equation that governs the dynamics of the APPA system. In particular, given the initial positions and velocities, the velocities of the particles are computed following Eq. (1). The new particle positions are then determined by Euler integration of the standard equation of motion. Specifically, the velocity of a particle $\mathbf{v}(t_i) = d\mathbf{r}/dt$ at time step t_i is evaluated over a sequence of K equally spaced time steps, i.e., $0 \leqslant i \leqslant K - 1$, between the initial time t_0 and final time t_f. The size of the time step $dt = t_{i+1} - t_i$ is fixed during the simulation and is chosen such that the average magnitude of the displacement $d\mathbf{r} = \mathbf{r}_{i+1} - \mathbf{r}_i$ between t_{i+1} and t_i is about $0.01R_c$ (i.e., about 1% of the particle radius). The change in $\mathbf{r}$ is the accumulated $d\mathbf{r}$ over all time steps.

Let $\mathbf{v}(t_i) = v_0\mathbf{e}$ denote the initial velocity of a particle at time t_i, where v_0 is the persistent speed and $\mathbf{e}$ is a unit vector characterizing the persistent direction. The position of the particle at time t_{i+1} is given by

$$\mathbf{r}(t_{i+1}) = \mathbf{r}(t_i) + v_0\mathbf{e}(t_i)dt + \sqrt{2D_t}\boldsymbol{\eta}(t_i)dt, \quad \text{(A1)}$$

which includes both a ballistic part and a diffusive part. The particle velocity is updated as follows. We first compute a temporal velocity $\mathbf{v}_{\text{temp}}$ using the current velocity $v_0\mathbf{e}(t_i)$ and the effects of ECM-mediated mechanical coupling, i.e.,

$$\mathbf{v}_{\text{temp}} = v_0\mathbf{e}(t_i) + \mu\mathbf{F}^{\text{ECM}}(t_i), \quad \text{(A2)}$$

where $\mathbf{F}^{\text{ECM}}(t_i)$ is computed based on the positions and velocities of particles at time t_i according to Eqs. (2) and (3). Next the persistent direction is updated:

$$\mathbf{e}(t_{i+1}) = \frac{\mathbf{v}_{\text{temp}}}{|\mathbf{v}_{\text{temp}}|}. \quad \text{(A3)}$$

Finally, the direction unit vector $\mathbf{e}(t_{i+1})$ specified by an angle $\boldsymbol{\theta}(t_{i+1})$ is updated following the Langevin equation, i.e.,

$$\boldsymbol{\theta}(t_{i+1}) = \boldsymbol{\theta}(t_i) + \sqrt{2D_r}\boldsymbol{\eta}(t_i)dt, \quad \text{(A4)}$$

where D_r is the rotational diffusivity. The new persistent velocity of the particle is then given by $v_0\mathbf{e}(t_{i+1})$, which is plugged in Eq. (A1) to compute the new positions, and the
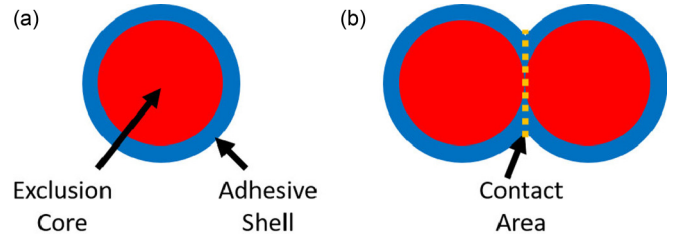

FIG. 12. Illustration for modeling cell-cell adhesion. (a) Each particle is composed of an exclusion core and an adhesive layer. (b) The adhesive layers can overlap and the adhesion force is proportional to the contact area.

new velocities are then updated according to Eqs. (A2)–(A4). These steps are repeated for all particles and all time steps.

APPENDIX B: EFFECTS OF CELL-CELL CONTACT ADHESION

In order to study the effects of cell-cell contact adhesion on the collective migration dynamics of the multicellular systems, which was not explicitly incorporated in our primary APPA model, we modify the APPA model to add an adhesive layer surrounding the exclusion core (see Fig. 12 for illustration). In particular, a particle includes two parts, i.e., the exclusion core and the adhesion shell (or layer). The radius of the particle core (same as the primary model $R_c = 10 \ \mu$m) and the thickness of the shell or layer ($\delta R_s = 0.15R_c$) are the same for all particles, which are selected based on confocal imaging data of contacting cell pairs. The adhesion shells of particles can overlap, while the cores cannot overlap as in
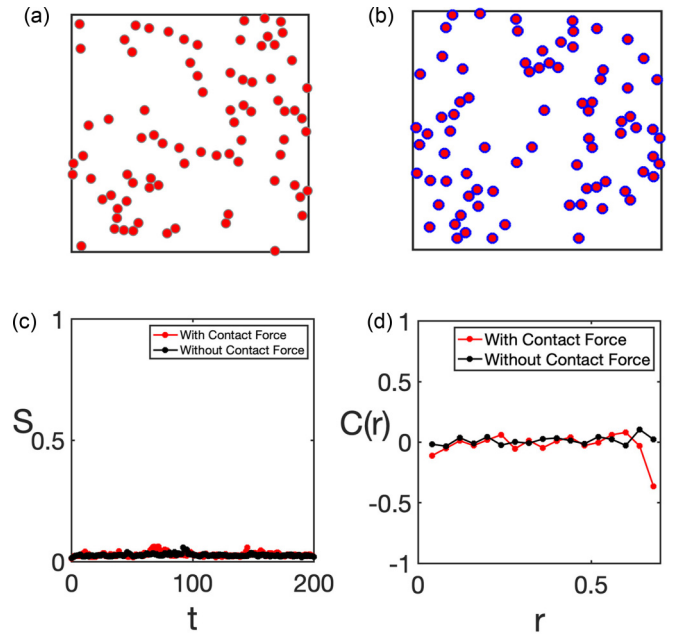

FIG. 13. Comparison of clustering dynamics resulting from the APPA model with and without cell-cell contact adhesion at $\rho = 0.1$ and $D_r = 0.05$. Snapshots show particle configurations (a) without and (b) with contact adhesion forces. Also shown are (c) the cluster statistics S and (d) the velocity correlation function $C(r)$.
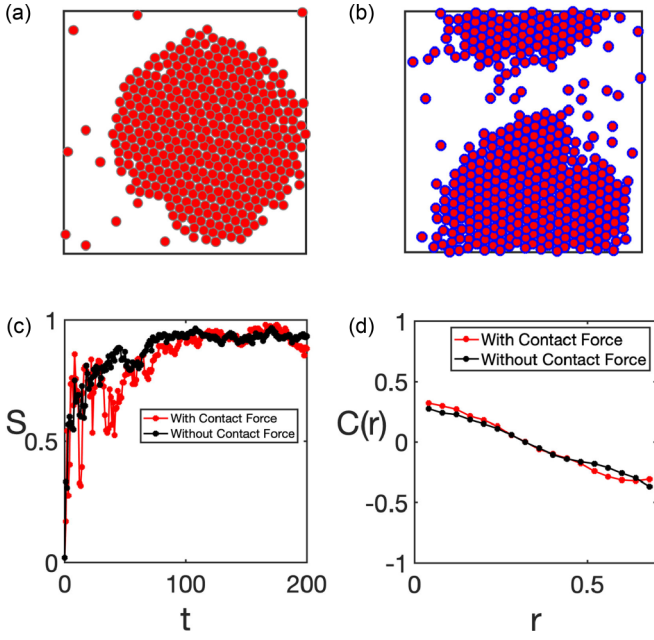
FIG. 14. Comparison of clustering dynamics resulting from the APPA model with and without cell-cell contact adhesion at $\rho = 0.5$ and $D_r = 0.05$. Snapshots show particle configurations (a) without and (b) with contact adhesion forces. Also shown are (c) the cluster statistics S and (d) the velocity correlation function $C(r)$.

FIG. 15. Comparison of clustering dynamics resulting from the APPA model with and without cell-cell contact adhesion at $\rho = 0.1$ and $D_r = 0.01$. Snapshots show particle configurations (a) without and (b) with contact adhesion forces. Also shown are (c) the cluster statistics S and (d) the velocity correlation function $C(r)$.

the primary model. When particle shells overlap, there is an attractive force between the centers of the particles, which is given by

$$\mathbf{F}^a(r) = k_a(2R_s - r)\mathbf{d}_0, \tag{B1}$$

where $R_s = R_c + \delta R_s$ is the radius of the shell, r is the distance between the centers of the two particles, $\mathbf{d}_0$ is the unit directional vector of the attraction, and k_a is the coefficient of the attractive force. The motion of particles is described by the overdamped Langevin equation in the form

$$\dot{\mathbf{r}}_i(t) = v_0\mathbf{e}_i + \mu\mathbf{F}_i^{\mathrm{ECM}} + \sqrt{2D_t}\,\boldsymbol{\eta}_i(t) + \mu\mathbf{F}_i^a, \tag{B2}$$

which is numerically integrated using the same procedure described in Appendix A.

Figures 12–16 show a comparison of the clustering dynamics at low and high cell densities $\rho = 0.1$ and 0.5, respectively, in systems with and without contact adhesion forces, and at different rotational diffusivities D_r. It can be seen that although at low densities, adhesion tends to better stabilize small clusters and the dynamics of the systems as quantified by cluster statistics and velocity correlation functions are almost the same.

One possible explanation is that the activity of the particles is sufficient to stabilize large clusters at sufficiently high local density. For example, two particles migrating toward each other and forming a cluster can only separate when their persistent velocity directions are both changed to the opposite directions. Therefore, incorporating contact adhesion, at least in the present model, does not seem to significantly influence the aggregation dynamics. We also realize that the current model for modeling cell-cell adhesion might not be the ideal and most accurate one to capture the collective dynamics of
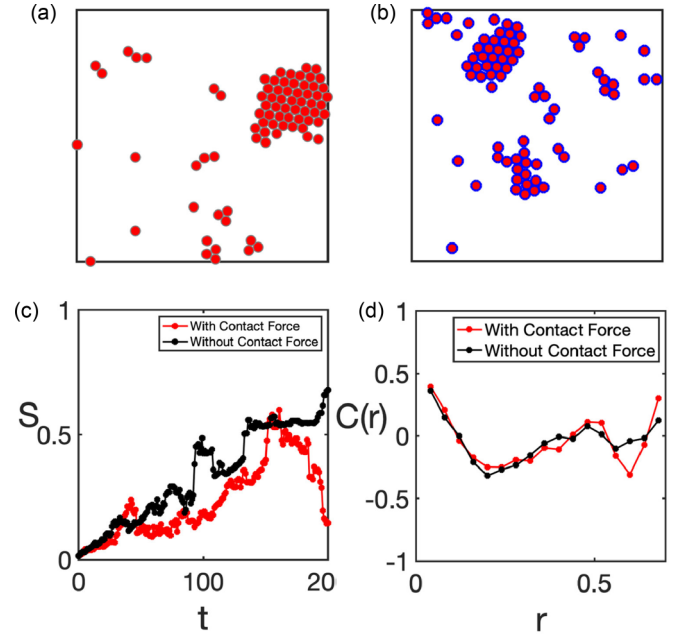
cell clusters, for which the vertex-based models would be more appropriate. We expect that increasing the strength of adhesion would enhance the rate of clustering, but would not qualitatively change the aggregation behaviors.
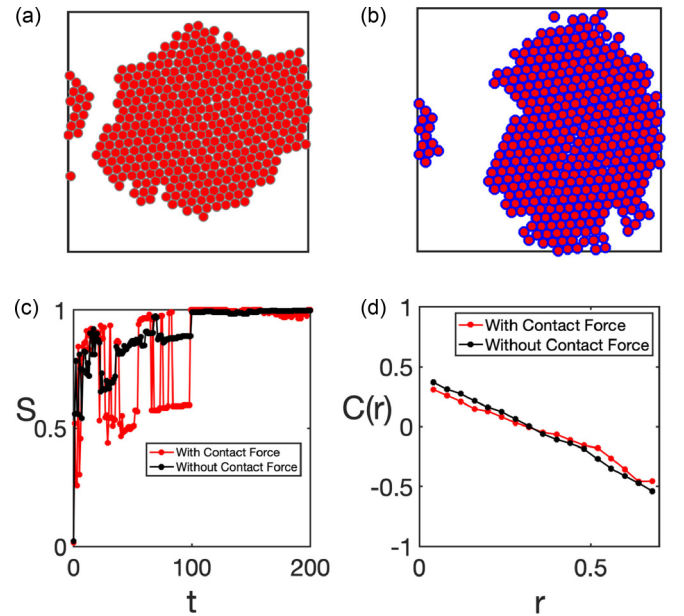

FIG. 16. Comparison of clustering dynamics resulting from the APPA model with and without cell-cell contact adhesion at $\rho = 0.5$ and $D_r = 0.01$. Snapshots show particle configurations (a) without and (b) with contact adhesion forces. Also shown are (c) the cluster statistics S and (d) velocity correlation function $C(r)$.

[1] A. J. Ridley, M. A. Schwartz, K. Burridge, R. A. Firtel, M. H. Ginsberg, G. Borisy, J. T. Parsons, and A. R. Horwitz, Cell migration: Integrating signals from front to back, Science **302**, 1704 (2003).

[2] P. Friedl and E.-B. Brocker, The biology of cell locomotion within three-dimensional extracellular matrix, Cell. Mol. Life Sci. **57**, 41 (2000).

[3] A. Aman and T. Piotrowski, Cell migration during morphogenesis, Dev. Biol. **341**, 20 (2010).

[4] P. Friedl and D. Gilmour, Collective cell migration in morphogenesis, regeneration and cancer, Nat. Rev. Mol. Cell Biol. **10**, 445 (2009).

[5] A. Vaezi, C. Bauer, V. Vasioukhin, and E. Fuchs, Actin cable dynamics and Rho/Rock orchestrate a polarized cytoskeletal architecture in the early steps of assembling a stratified epithelium, Dev. Cell **3**, 367 (2002).

[6] S. Werner, T. Krieg, and H. Smola, Keratinocyte fibroblast interactions in wound healing, J. Invest. Dermatol. **127**, 998 (2007).

[7] H. Szurmant and G. W. Ordal, Diversity in chemotaxis mechanisms among the bacteria and archaea, Microbiol. Mol. Biol. Rev. **68**, 301 (2004).

[8] S. V. Plotnikov, A. M. Pasapera, B. Sabass, and C. M. Waterman, Force fluctuations within focal adhesions mediate ECM-rigidity sensing to guide directed cell migration, Cell **151**, 1513 (2012).

[9] R. Sunyer, V. Conte, J. Escribano, A. Elosegui-Artola, A. Labernadie, L. Valon, D. Navajas, J. M. García-Aznar, J. J. Muñoz, P. Roca-Cusachs, and X. Trepat, Collective cell durotaxis emerges from long-range intercellular force transmission, Science **353**, 1157 (2016).

[10] E. Hadjipanayi, V. Mudera, and R. A. Brown, Guiding cell migration in 3D: A collagen matrix with graded directional stiffness, Cell Motil. Cytoskel. **66**, 121 (2009).

[11] S. B. Carter, Haptotaxis and the mechanism of cell motility, Nature (London) **213**, 256 (1967).

[12] P. P. Provenzano, D. R. Inman, K. W. Eliceiri, S. M. Trier, and P. J. Keely, Contact guidance mediated three-dimensional cell migration is regulated by Rho/ROCK-dependent matrix reorganization, Biophys. J. **95**, 5374 (2008).

[13] J. H. Wang and E. S. Grood, The strain magnitude and contact guidance determine orientation response of fibroblasts to cyclic substrate strains, Connect. Tissue Res. **41**, 29 (2000).

[14] S. Guido and R. T. Tranquillo, A methodology for the systematic and quantitative study of cell contact guidance in oriented collagen gels. Correlation of fibroblast orientation and gel birefringence, J. Cell Sci. **105**, 317 (1993).

[15] R. Ananthakrishnan and A. Ehrlicher, The forces behind cell movement, Int. J. Biol. Sci. **3**, 303 (2007).

[16] M. J. Footer, J. W. J. Kerssemakers, J. A. Theriot, and M. Dogterom, Direct measurement of force generation by actin filament polymerization using an optical trap, Proc. Natl. Acad. Sci. **104**, 2181 (2007).

[17] S. Wang and P. G. Wolynes, Active contractility in actomyosin networks, Proc. Natl. Acad. Sci. **109**, 6446 (2012).

[18] T. Lecuit, P.-F. Lenne, and E. Munro, Force generation, transmission, and integration during cell and tissue morphogenesis, Annu. Rev. Cell Dev. Biol. **27**, 157 (2011).

[19] M. A. Schwartz, Integrins and extracellular matrix in mechanotransduction, Cold Spring Harb. Perspect. Biol. **2**, a005066 (2010).

[20] G. Totsukawa, Y. Wu, Y. Sasaki, D. J. Hartshorne, Y. Yamakita, S. Yamashiro, and F. Matsumura, Distinct roles of MLCK and ROCK in the regulation of membrane protrusions and focal adhesion dynamics during cell migration of fibroblasts, J. Cell Biol. **164**, 427 (2004).

[21] C. A. R. Jones, M. Cibula, J. Feng, E. A. Krnacik, D. H. McIntyre, H. Levine, and B. Sun, Micromechanics of cellularized biopolymer networks, Proc. Natl. Acad. Sci. **112**, E5117 (2015).

[22] S. B. Lindstrom, D. A. Vader, A. Kulachenko, and D. A. Weitz, Biopolymer network geometries: Characterization, regeneration, and elastic properties, Phys. Rev. E **82**, 051905 (2010).

[23] H. Mohammadi, P. D. Arora, C. A. Simmons, P. A. Janmey, and C. A. McCulloch, Inelastic behavior of collagen networks in cell-matrix interactions and mechanosensation, J. R. Soc. Interface **12**, 20141074 (2015).

[24] S. Nam, K. H. Hu, M. J. Butte, and O. Chaudhuri, Strain-enhanced stress relaxation impacts nonlinear elasticity in collagen gels, Proc. Natl. Acad. Sci. **113**, 5492 (2016).

[25] J. Kim, J. Feng, C. A. Jones, X. Mao, L. M. Sander, H. Levine, and B. Sun, Stress-induced plasticity of dynamic collagen networks, Nat. Commun. **8**, 842 (2017).

[26] S. Chen, W. Xu, J. Kim, H. Nan, Y. Zheng, B. Sun, and Y. Jiao, Novel inverse finite-element formulation for reconstruction of relative local stiffness in heterogeneous extra-cellular matrix and traction forces on active cells, Phys. Biol. **16**, 036002 (2019).

[27] A. D. Doyle, N. Carvajal, A. Jin, K. Matsumoto, and K. M. Yamada, Local 3D matrix microenvironment regulates cell migration through spatiotemporal dynamics of contractility-dependent adhesions, Nat. Commun. **6**, 8720 (2015).

[28] Y. L. Han, P. Ronceray, G. Xu, A. Malandrino, R. D. Kamm, M. Lenz, C. P. Broedersz, and M. Guo, Cell contraction induces long-ranged stress stiffening in the extracellular matrix, Proc. Natl. Acad. Sci. **115**, 4075 (2018).

[29] X. Ma, M. E. Schickel, M. D. Stevenson, A. L. Sarang-Sieminski, K. J. Gooch, S. N. Ghadiali, and R. T. Hart, Fibers in the extracellular matrix enable long-range stress transmission between cells, Biophys. J. **104**, 1410 (2013).

[30] P. Ronceray, C. P. Broedersz, and M. Lenz, Fiber networks amplify active stress, Proc. Natl. Acad. Sci. **113**, 2827 (2016).

[31] H. Wang, A. S. Abhilash, C. S. Chen, R. G. Wells, and V. B. Shenoy, Long-range force transmission in fibrous matrices enabled by tension-driven alignment of fibers, Biophys. J. **107**, 2592 (2014).

[32] L. Liang, C. Jones, S. Chen, B. Sun, and Y. Jiao, Heterogeneous force network in 3D cellularized collagen networks, Phys. Biol. **13**, 066001 (2016).

[33] F. Beroz, L. M. Jawerth, S. Munster, D. A. Weitz, C. P. Broedersz, and N. S. Wingreen, Physical limits to biomechanical sensing in disordered fibre networks, Nat. Commun. **8**, 16096 (2017).

[34] H. Nan, Y. Zheng, Y. H. Lin, S. Chen, C. Z. Eddy, J. Tian, W. Xu, B. Sun, and Y. Jiao, Absorbing-active transition in multi-cellular system regulated by dynamic force network, Soft Matter **15**, 6938 (2019).

[35] A. A. Alobaidi, Y. Xu, Y. Jiao, and B. Sun, Probing cooperative force generation in collective cancer invasion, Phys. Biol. **14**, 045005 (2017).

[36] Y. Zheng, H. Nan, Y. Liu, Q. Fan, X. Wang, R. Liu, L. Liu, F. Ye, B. Sun, and Y. Jiao, Modeling cell migration regulated by cell-extracellular-matrix micromechanical coupling, Phys. Rev. E **100**, 043303 (2019).

[37] J. Kim, Y. Zheng, A. A. Alobaidi, H. Nan, J. Tian, Y. Jiao, and B. Sun, Geometric dependence of three-dimensional collective cancer invasion, Biophys. J. **118**, 1177 (2020).

[38] M. H. Zaman, R. D. Kamm, P. Matsudaira, and D. A. Lauffenburger, Computational model for cell migration in three-dimensional matrices, Biophys. J. **89**, 1389 (2005).

[39] A. Vaziri and A. Gopinath, Cell and biomolecular mechanics *in silico*, Nat. Mater. **7**, 15 (2008).

[40] P. Masuzzo, M. Van Troys, C. Ampe, and L. Martens, Taking aim at moving targets in computational cell migration, Trends Cell Biol. **26**, 88 (2016).

[41] F. Ziebert, S. Swaminathan, and I. S. Aranson, Modeling for self-polarization and motility of keratocyte fragments, J. R. Soc. Interface **9**, 1084 (2011).

[42] D. Shao, W. J. Rappel, and H. Levine, Computational Model for Cell Morphodynamics, Phys. Rev. Lett. **105**, 108104 (2010).

[43] D. Shao, H. Levine, and W. J. Rappel, Coupling actin flow, adhesion, and morphology in a computational cell motility model, Proc. Natl. Acad. Sci. USA **109**, 6851 (2012).

[44] U. Z. George, A. Stephanou, and A. Madzvamuse, Mathematical modeling and numerical simulations of actin dynamics in the eukaryotic cell, J. Math. Biol. **66**, 547 (2013).

[45] T. C. Bidone, W. Jung, D. Maruri, C. Borau, R. D. Kamm, and T. Kim, Morphological transformation and force generation of active cytoskeletal networks, PLoS Comput. Biol. **13**, e1005277 (2017).

[46] M. C. Kim, J. Whisler, Y. R. Silberberg *et al.*, Cell invasion dynamics into a three dimensional extracellular matrix fibre network, PLoS Comput. Biol. **11**, e1004535 (2015).

[47] D. Bi, J. Lopez, J. Schwarz, and M. L. Manning, A density-independent rigidity transition in biological tissues, Nat. Phys. **11**, 1074 (2015).

[48] F. Graner and J. A. Glazier, Simulation of Biological Cell Sorting Using a Two-Dimensional Extended Potts Model, Phys. Rev. Lett. **69**, 2013 (1992).

[49] Y. Jiao and S. Torquato, Emergent properties from a cellular automaton model for invasive tumor growth in heterogeneous environment, PLoS Comput. Biol. **7**, 1002314 (2011).

[50] Y. Jiao and S. Torquato, Diversity of dynamics and morphologies of invasive solid tumors, AIP Adv. **2**, 011003 (2012).

[51] Y. Jiao and S. Torquato, Evolution and morphology of microenvironment-enhanced malignancy of three-dimensional invasive solid tumors, Phys. Rev. E **87**, 052707 (2013).

[52] H. Xie, Y. Jiao, Q. Fan *et al.*, Modeling three-dimensional invasive solid tumor growth in heterogeneous microenvironment under chemotherapy, PLoS One **13**, e0206292 (2018).

[53] J. Lober, F. Ziebert, and I. S. Aranson, Modeling crawling cell movement on soft engineered substrates, Soft Matter **10**, 1365 (2014).

[54] J. Lober, F. Ziebert, and I. S. Aranson, Collisions of deformable cells lead to collective migration, Sci. Rep. **5**, 9172 (2015).

[55] A. Goychuk, D. B. Bruckner, A. W. Holle, J. P. Spatz, C. P. Broedersz, and E. Frey, Morphology and motility of cells on soft substrates, arXiv:1808.00314.

[56] J. Zhu and A. Mogilner, Comparison of cell migration mechanical strategies in three-dimensional matrices: A computational study, Interface Focus **6**, 20160040 (2016).

[57] A. Moure and H. Gomez, Phase-field model of cellular migration: Three-dimensional simulations in fibrous networks, Comput. Methods Appl. Mech. Eng. **320**, 162 (2017).

[58] A. Moure and H. Gomez, Three-dimensional simulation of obstacle-mediated chemotaxis, Biomech. Model. Mechanobiol. **17**, 1243 (2018).

[59] H. Abdel-Rahman, B. Thomas, and T. Kim, A mechanical model for durotactic cell migration, ACS Biomater. Sci. Eng. **5**, 3954 (2019).

[60] M. Dietrich, H. Le Roy, D. B. Bruckner, H. Engelke, R. Zantl, J. O. Radler, and C. P. Broedersz, Guiding 3D cell migration in deformed synthetic hydrogel microstructures, Soft Matter **14**, 2816 (2018).

[61] M. F. Staddon, D. Bi, A. P. Tabatabai, V. Ajeti, M. P. Murrell, and S. Banerjee, Cooperation of dual modes of cell motility promotes epithelial stress relaxation to accelerate wound healing, PLoS Comput. Biol. **14**, e1006502 (2018).

[62] V. Ajeti, A. P. Tabatabai, A. J. Fleszar, M. F. Staddon, D. S. Seara, C. Suarez, M. S. Yousafzai, D. Bi, D. R. Kovar, S. Banerjee, and M. P. Murrell, Wound healing coordinates actin architectures to regulate mechanical work, Nat. Phys. **15**, 696 (2019).

[63] E. N. Schaumanna, M. F. Staddon, M. L. Gardel, and S. Banerjee, Force localization modes in dynamic epithelial colonies, Mol. Biol. Cell **29**, 2835 (2018).

[64] J. Feng, H. Levine, X. Mao, and L. Sander, Stiffness sensing and cell motility: Durotaxis and contact guidance (unpublished).

[65] T. Vicsek, A. Czirok, E. Ben-Jacob, I. Cohen, and O. Shochet, Novel Type of Phase Transition in a System of Self-Driven Particles, Phys. Rev. Lett. **75**, 1226 (1995).

[66] J. M. Belmonte, G. L. Thomas, L. G. Brunnet, R. M. C. de Almeida, and H. Chaté, Self-Propelled Particle Model for Cell-Sorting Phenomena, Phys. Rev. Lett. **100**, 248702 (2008).

[67] X. Yang, M. L. Manning, and M. C. Marchetti, Aggregation and segregation of confined active particles, Soft Matter **10**, 6477 (2014).

[68] R. Ni, M. A. C. Stuart, and P. G. Bolhuis, Tunable Long Range Forces Mediated by Self-Propelled Colloidal Hard Spheres, Phys. Rev. Lett. **114**, 018302 (2015).

[69] Z. Preisler and M. Dijkstra, Configurational entropy and effective temperature in systems of active Brownian particles, Soft Matter **12**, 6043 (2016).

[70] C. Bechinger, R. Di Leonardo, H. Lowen, C. Reichhardt, and G. Volpe, Active particles in complex and crowded environments, Rev. Mod. Phys. **88**, 045006 (2016).

[71] H. Nan, L. Liang, G. Chen, L. Liu, R. Liu, and Y. Jiao, Realizations of highly heterogeneous collagen networks via stochastic reconstruction for micromechanical analysis of tumor cell invasion, Phys. Rev. E **97**, 033311 (2018).

[72] C. Jones, L. Liang, D. Lin, Y. Jiao, and B. Sun, The spatial-temporal characteristics of type I collagen-based extracellular matrix, Soft Matter **10**, 8855 (2014).

[73] S. Kirkpatrick, C. D. Gelatt, and M. P. Vecchi, Optimization by simulated annealing, Science **220**, 671 (1983).

[74] Y. Shokef and S. A. Safran, Scaling Laws for the Response of Nonlinear Elastic Media with Implications for Cell Mechanics, Phys. Rev. Lett. **108**, 178103 (2012).

[75] J. Steinwachs, C. Metzner, K. Skodzek, N. Lang, I. Thievessen, C. Mark, S. Münster, K. E. Aifantis, and B. Fabry, Three-dimensional force microscopy of cells in biopolymer networks, Nat. Methods **13**, 171 (2016).

[76] B. Burkel, M. Proestaki, S. Tyznik, and J. Notbohm, Heterogeneity and nonaffinity of cell-induced matrix displacements, Phys. Rev. E **98**, 052410 (2018).

[77] S. Tyznik and J. Notbohm, Length scale dependent elasticity in random three-dimensional fiber networks, Mech. Mater. **138**, 103155 (2019).

[78] See Supplemental Material at http://link.aps.org/supplemental/10.1103/PhysRevE.102.052409 for details.

[79] S. Torquato and Y. Jiao, Effect of dimensionality on the continuum percolation of overlapping hyperspheres and hypercubes. II. Simulations and analyses, J. Chem. Phys. **137**, 074106 (2012).

[80] S. Torquato and Y. Jiao, Effect of dimensionality on the percolation threshold of anisotropic overlapping particles, Phys. Rev. E **87**, 022111 (2013).

[81] S. Torquato and Y. Jiao, Effect of dimensionality on the percolation thresholds of various d-dimensional lattices, Phys. Rev. E **87**, 032149 (2013).

[82] K. Wolf, S. Alexander, V. Schacht, L. M. Coussens, U. von Andrian, J. van Rheenen, E. Deryugina, and P. Friedl, Collagen-based cell migration models in vitro and in vivo, Semin. Cell Dev. Biol. **20**, 931 (2009).

[83] K. Wolf, M. te Lindert, M. Krause, S. Alexander, J. te Riet, A. L. Willis, R. M. Hoffman, C. G. Figdor, S. J. Weiss, and P. Friedl, Physical limits of cell migration: Control by ECM space and nuclear deformation and tuning by proteolysis and traction force, J. Cell Biol. **201**, 1069 (2013).

[84] W. Han, S. Chen, W. Yuan, Q. Fan, J. Tian, X. Wang, L. Chen, X. Zhang, W. Wei, R. Liu, J. Qu, Y. Jiao, R. H. Austin, and L. Liu, Oriented collagen fibers direct tumor cell intravasation, Proc. Natl. Acad. Sci. USA **113**, 11208 (2016).